Particle size distributions and hygroscopic restructuring of ultrafine particles emitted during thermal spraying

A. Salmatonidis[1,2], M. Viana[1], G. Biskos[3,4], S. Bezantakos[3,5]*

*Corresponding author: S. Bezantakos

[1]Institute of Environmental Assessment and Water Research (IDAEA-CSIC), Barcelona, Spain

[2]Department of Chemical Engineering and Analytical Chemistry, Faculty of Chemistry, University of Barcelona, Barcelona, Spain

[3]Energy Environment and Water Research Centre, The Cyprus Institute, Nicosia, Cyprus

[4]Faculty of Civil Engineering and Geosciences, Delft University of Technology, Delft, The Netherlands

[5]Université du Littoral Côte d' 'Opale, Dunkerque, France

Abstract

We report measurements of the size, concentration, and hygroscopicity of ultrafine particles (UFPs) emitted during thermal spraying of ceramic coatings in an industrial setting. High concentrations (i.e., higher than 10^6 cm^{-3}) of fractal-like UFPs were measured inside the spraying booths of the facility. The emitted UFPs were found to take up small amounts of water when exposed to elevated relative humidity (RH = 87%) within a Hygroscopic Tandem Differential Mobility Analyzer (HTDMA) system. The hygroscopicity of the sampled particles was distinguishably lower compared to those of the atmospheric background aerosol particles present in the breathing air. UFPs smaller than 90 nm that are produced by the thermal spraying process, exhibit hygroscopic factors less than unity in a systematic way. This behaviour indicates that the particles were irregularly shaped at dry conditions, and that they underwent a shape change (i.e., restructuring) upon humidification inside the HTDMA. The fractal-like structure of process-emitted UFPs was further corroborated by Transmission Electron Microscopy (TEM) conducted on samples collected on site at dry conditions.

Keywords: In-situ characterization; Health risk; Ceramic nanoparticles; Workplace emission hygroscopicity; Fractal-like particles hygroscopicity

1. Introduction

Release of airborne particles in the workplace air has become an issue of growing concern with regard to worker exposure (Pietroiusti et al., 2018; Viitanen et al., 2017), as a result of the well-established adverse respiratory and cardiovascular impacts of ultrafine, fine and coarse particles (Oberdörster, 2001; World Health Organization, 2016; Gakidou et al., 2017; Landrigan, 2017). Ultrafine particles (UFPs), which entail the highest risks, may be unintentionally emitted during different industrial processes such as welding (Zhang et al., 2013), ceramic tile sintering (Fonseca et al., 2016), atmospheric plasma spraying (Salmatonidis et al., 2019), laser ablation (Salmatonidis et al., 2018), or iron casting (van Broekhuizen, 2017). Thermal spraying processes, such as atmospheric plasma spraying (APS) and High Velocity Oxy-fuel (HVOF) have been associated with high UFP emissions (Salmatonidis et al., 2019). Unintentional release of UFPs in industrial settings frequently results in high exposure concentrations, which contrast with relatively low background particle concentrations (Fonseca et al., 2015; Dahmann, 2016; van Broekhuizen, 2017). Nevertheless, distinguishing between the two particle populations based on their intrinsic properties, is of primary importance for assessing their potential toxicological and health impacts (Ganguly et al., 2018; Limbach et al., 2007; Song et al., 2009).

Discriminating unintentionally-released UFPs – also referred to as process-generated or incidental nanoparticles – from background aerosol particles using methods based on spatially or temporally distributed observations are already reported in the literature (Kuhlbusch et al., 2011, 2009; Schill and Chosewood, 2013; OECD, 2015; Asbach et al., 2016; Dahmann, 2016). Most of these methods employ instruments to quantify background and UFP sources in terms of aerosol metrics such as particle number or mass concentrations (Ono-Ogasawara et al., 2009; Peters et al., 2009; Asbach et al., 2012), but not based on intrinsic particle properties such as morphology. This is mainly due to the fact that most of the instruments available for exposure monitoring employ these metrics (Asbach et al., 2016), posing a challenge for source identification and distinction of process-generated from background aerosol particles; something that state-of-the-art aerosol instrumentation can achieve (Kalantzi and Biskos, 2014).

Apart from the concentration of UFPs, having information of their size distribution and hygroscopic behavior is key to understand their impacts upon human health. This is because these are two intrinsic properties that define the deposition efficiency of inhaled particles in the human

respiratory system (Löndahl et al., 2007; Ching and Kajino, 2018). The size of the inhaled particle affects directly their deposition efficiency in the different parts of the respiratory system, whereas the hygroscopicity can have an indirect effect as it can change the size and morphology of the particles within the respiratory system. In fact, aerosol hygroscopicity plays a significant role given that inhaled particles are exposed to relative humidity (RH) levels close to 99% in the human respiratory system (Anselm et al., 1990; Ferron et al., 1988), at which the size and structure, and consequently the deposition patterns, of the particles can change (Löndahl et al., 2007). The mixing state of the inhaled aerosol also plays an important role on particle deposition in the human respiratory system, and consequently on the associated health effects. In externally mixed aerosols, particles having the same size at dry conditions but different composition, will grow to different sizes, and therefore exhibit different deposition pattern, upon inhalation. Along these lines, it has been shown that the deposition of externally mixed fresh hydrophobic soot particles, found in urban plumes, in the alveolar region can be underestimated by 5 to 20% if treated as internally mixed with more hygroscopic background aerosols (Ching and Kajino, 2018).

An additional motive for probing the hygroscopic behavior of aerosol particles is that it can be used as a metrics to identify particles with irregular morphology (i.e., fractal-like particles) as their shape can change from that of open to more compact structures at elevated relative humidity (RH) conditions during the measurements. This phenomenon is manifested as an apparent shrinking of the particles when exposed to elevated RH, which can significantly affect other size/shape related metrics (e.g., their Lung Deposition Surface Area; Asbach et al., 2017). Observations of restructuring upon humidification have been reported for non-spherical but hygroscopic particles (e.g., sodium chloride particles; Krämer et al., 2000; Biskos et al., 2006a), as well as for hydrophobic non-spherical fractal-like particles (e.g., soot particles; Weingartner et al., 1995; Tritscher et al., 2011).

In this work we report on measurements of the size distribution of UFPs emitted at a thermal spraying facility under real-world operating conditions. In addition, we use a Hygroscopic Tandem Differential Mobility Analyzer (HTDMA; Rader and McMurry, 1986) to probe the hygroscopic behavior (i.e., the ability to take up water and restructure upon exposure to elevated water vapor concentrations), as well as the mixing state of the UFPs in the collected samples. Transmission electron microscopy (TEM) grids were used to sample the emitted particles in order to verify that

they had irregular shapes at dry conditions and to determine their chemical composition (using Energy Dissipative X-ray Spectroscopy; EDX).

2. Experimental

Particle concentrations and hygroscopicities were monitored during thermal spraying at an industrial-scale precision engineering workshop (T.M. Comas, Blanes, Spain). The measurements were carried out over a 4-day period, and were representative of the usual operating conditions in the plant. Although data were collected and analysed during the whole duration of the campaign, in this study only selected cases are presented which are representative of the described thermal spraying processes.

The facility had three thermal spraying booths located in an area of approximately 240 m^2 (14 m wide and 17 m in length) that includes a central area and it's described in detail elsewhere (Salmatonidis et al., 2019). Different spraying techniques were used in each of the booths (cf. Figure S1 in the Supplementary Information; SI). Booth #1 housed an Atmospheric Plasma Spraying (APS) system, characterised by high temperatures (5-20×10^3 ºC) and relatively low projection velocities (200-500 m/s), that was used to spray TiO_2-Al_2O_3 or Cr-Ni powder blends with mean grain diameters of 36.0 and 76.5 μm, respectively. At the very high temperatures that are developed during APS, the feedstock is melted and driven through the formed jet towards the workpiece, i.e., the surface being coated (Pawlowski, 2008). The metal vapors are oxidized by entrained air and condense in the cold zone of the jet (Fauchais et al., 2001; Mauer et al., 2011; Planche et al., 2003) between the plasma gun and the workpiece; a mechanism that results in nanoparticle formation (cf. Figure S2a). According to this mechanism, the primary nanoparticles emitted by APS should principally have spherical shapes as they mainly originate from condensation of gaseous or liquid precursors.

The other spraying booth (Booth #3, cf. Figure S1) housed a High Velocity Oxy-Fuel (HVOF) coating spraying system, characterised by high spraying velocities (425-1500 m/s) and lower temperatures (2.9×10^3 ºC), in which a WC-Cr_3C_2-Ni powder blend (mean grain diameter of 34 μm) was used as feedstock. During HVOF, feedstock particles with high kinetic energies are sprayed onto the metal surface of the workpiece. In this case the feedstock material is not entirely melted as the temperatures are relatively lower, and it is driven with supersonic speeds towards the workpiece (Pawlowski, 2008). Microscaled particles are in a solid-liquid two-phase droplet

state when impacting on their target, and thus are flattened during deposition (Li et al., 2004). Consequently, particles emitted from the HVOF system are expected to have irregular shapes (cf. Figure S2b). An additional emission route of submicron particles could be fugitive streams containing particles that would not be deposited on the substrate as they would simply disperse inside the booth (Li and Christofides, 2006).

2.1 Monitoring locations and instrumentation

Particle concentrations, size distributions and hygroscopicities were monitored inside two spraying booths (#1 and #3), where workers used respiratory protective equipment. The temperature of the air sampled throughout the campaign was in the range of 20-25 ºC. The following particle monitoring instrumentation was deployed:

- A custom-made HTDMA system (cf. Figure S3 in the SI) was used to measure the hygroscopicity of the sampled particles. The instrument consisted of two custom-made Differential Mobility Analyzers (DMAs; Knutson and Whitby, 1975) and a Condensation Particle Counter (CPC; TSI 3010 CPC; Agarwal and Sem, 1980). The first DMA (DMA-1) of the system was used for selecting nearly monodisperse dried particles, which were then exposed to elevated RH conditions before their size distribution was measured by the second DMA (DMA-2) and the CPC (cf. more details in SI). A silica gel diffusion drier was employed upstream DMA-1 of the HTDMA in order to secure that all selected particles are in dry conditions, maintaining the RH below 30%. The system was operated with sheath and aerosol flow rates of 3.0 and 0.3 L/min, respectively, and for both of them the RH was controlled to 87% in order to avoid RH non-uniformities through the systems that can lead to experimental artefacts (cf. SI; Biskos et al., 2006b; Bezantakos et al., 2016). The sampling time of the instrument was 180 s, and the voltage of DMA-1 was changed every 6 minutes (i.e., every two sampling periods) in order to sequentially select particles having dry electrical mobility diameters of either 30 or 90 nm. These sizes were selected as they reside to the most commonly observed size range of particles emitted during thermal plasma spraying processes (i.e., $Mode_{26\text{-}90}$; cf. Salmatonidis et al., 2019), while differing by a factor of 3 (i.e., in terms of size), thus enhancing the probability of observing any potential size-related differences. The instrument was deployed in the worker area, sampling directly from spraying booths #1 and

#3, except from a short period of ca. 2 hours before the end of the campaign during which it sampled from the central area outside booth #3.

- A NanoScan Scanning Mobility Particle Sizer (NanoScan-SMPS; TSI Model 3910), was used to measure the particle size distribution (10-420 nm) in 13 channels with a 1-min time resolution. Similarly to the HTDMA, the NanoScan-SMPS was in the worker area but was sampling inside the spraying booths through 3-m long conductive tubing inlets. The NanoScan-SMPS raw data were converted to number-based mobility particle size distributions using the Multi-Instrument Manager software (MIM; TSI). In addition, particle number concentrations (dN) reported by the instrument at each size channel (dp) were corrected, accounting for the diffusion losses in the sampling lines (Hinds, 1999).
- A particle sampling system comprising a cassette (SKC, inlet diameter 1/8 inch) housing transmission electron microscope (TEM) grids attached on filter support pads (25 mm in diameter), was used to collect particles for offline characterisation. The system employed an SKC Leland pump that was operated at a flow of 5 L/min. The grids (Agar Scientific Quantifoil 200 Mesh Au) were analysed offline for morphological and physicochemical particle characterisation using a TEM (Jeol, JEM 1220, Tokyo, Japan) coupled with an Energy-Dispersive X-ray (EDX; Oxford Instruments) spectrometer, following a similar procedure as described elsewhere (Voliotis et al., 2014). Samples were collected inside all the spraying booths, while TEM images were processed by the "ImageJ" software, version 1.52f. In order to determine the size of particles a spherical shape was assumed. The diameter of a particle was defined as the larger distance of two antidiametric points on the surface of the particle connected by a straight line. TEM was used to characterize the morphology and size of the emitted particles and it was not intended to get correlated with concentration factors.

2.2 Assessment of particles hygroscopicity, mixing state, and dynamic shape factor

The hygroscopic behavior of aerosol particles, sampled by the HTDMA and exposed to high RH conditions, can be expressed by their hygroscopic factor:

$$g(\mathrm{RH}) = \frac{d_m(\mathrm{RH})}{d_{m,dry}} \quad , \qquad (1)$$

where d_m(RH) and $d_{m,dry}$ are the geometric mean mobility diameters of the sampled particles at the elevated RH (87%), measured by DMA-2 and the CPC, and at the dry state, determined as the mobility diameter selected by DMA-1, respectively (cf. SI for more details). Dried, internally mixed particles sampled by the HTDMA and exposed to the elevated RH conditions in the humidifier of the system grow (or apparently may shrink) to the same sizes as a result of water uptake, exhibiting a unimodal size distribution when measured by DMA-2 and the CPC. On the other hand, externally mixed particles sampled by the system, may grow (or apparently shrink) to different sizes exhibiting either a wider unimodal or a bimodal size distribution in the measurements. To distinguish between internally and externally mixed aerosol particles sampled by the HTDMA we employed the "TDMAfit" algorithm (Bezantakos et al., 2013; McMurry and Stolzenburg, 1989). Figures 1 and 2 show example HTDMA measurements and derived g(87%) values.

"Figure 1"

"Figure 2"

The factor g is greater than unity when the particles grow upon exposure to the elevated RH conditions or less than unity when they exhibit apparent shrinking. Irregularly-shaped and hydrophobic particles exposed to elevated RH (87%) in the HTDMA will most likely appear to shrink, having g(RH) < 1 (cf. Figure 2). The reason for this behavior is that in the calculation of g(RH), the two electrical mobility diameters (i.e., d_{m}(RH) and $d_{\mathrm{m,dry}}$) correspond to spherical particles (cf. Equations S1-S3 in the SI). However, the drag force acting upon a migrating irregularly-shaped particle during classification in the DMA is higher than that of a spherical particle having the same volume, making them to be classified under stronger electric fields within the classifier compared to their compacted/restructured counterparts. Potential uncertainties in the measured growth factors due to differences in the charging efficiency between spherical and irregular-shaped particles are negligible in these sizes ranges (Marick M. M., 2008), and thus have been neglected in our analysis.

The dynamic shape factor of the particles sampled by the HTDMA can be derived by comparing the mobility diameter of the irregularly shaped particles selected by DMA-1 to that of the restructured particles (i.e., measured by DMA-2), assuming that their electrical mobility diameter

is equal to their volume equivalent diameter (i.e., assuming that they are spheres; $d_m(RH) = d_{ve}$), as follows:

$$\chi = \frac{C_c(d_m(RH))}{g(RH)C_c(d_{m,dry})} \quad (2)$$

Here $C_c(d_m(RH))$ and $C_c(d_{m,dry})$ denote the Cunningham slip correction factors that should be calculated using Eq. S3 in the SI, corresponding respectively to the electrical mobility diameter of the particles after humidification (i.e., $d_m(RH)$; measured by DMA-2 of the HTDMA) and at dry conditions (i.e., $d_{m,dry}$; selected by DMA-1 of the HTDMA).

3. Results and discussion

3.1 Particle number concentration and mean diameters

Figures 3a and 3b show time series of particle number concentrations and size distributions measured inside booths #1 (APS) and #3 (HVOF), respectively. The observed patterns reflect the particle emissions during the morning shift, a break for lunch (no activity), and finally the afternoon shift. Particle number concentrations showed a high temporal variability and reached concentrations larger than 10^6 cm^{-3} as measured by the NanoScan-SMPS. These high concentrations may cause an underestimation of the particle number concentration as a result of ion depletion by the sampled particles in the corona charger. However, the effects on sizing performance of the instrument are negligible, as indicated by the very similar particle sizes measured with the NanoScan-SMPS when sampling outside the spraying booths, where the number concentration was at least an order of magnitude lower (i.e., 10^5 cm^{-3}; Salmatonidis et al., 2019).

"Figure 3"

In all cases, emissions from the spraying processes yielded particles number concentrations that were significantly higher compared to those in the background air, which was in the order of 10^4 cm^{-3}. The variability in particle concentrations and sizes is the result of numerous factors such as fluctuations in the process (different spraying conditions, variations of the feedstock, etc.), opening/closing of doors (effecting air exchange inside the booths and consequently the physical mechanisms leading to particle growth), and worker movement inside the booth (also impacting air flows), among others.

The size distribution patterns were moderately irregular in booth #1 (cf. Figure 3a), with three peaks (one between 30 and 40 nm, one between 25 and 100 nm, and one from 100 to 200 nm) and total concentrations up to 5×10^6 cm^{-3} being observed during the first spraying operation (Figure 3a, min 20-70). During the second repetition, the total particle concentration was lower (ca. 2.5×10^6 cm^{-3}), while the mean particle diameter ranged between 40 and 100 nm. In booth #3, total particle number concentrations reached ca. 5×10^6 cm^{-3} in each repetition, with their mean diameters being in the range of 40-80 nm (cf. Figure 3b). The emission patterns, especially in booth #3, were comparable across the different repetitions of the spraying process. Variation of the emissions patterns observed during spraying in booth #1 were attributed to the sequence of the activities followed in this process (Salmatonidis et al., 2019), where different feedstock materials were used to create different layers of coatings on the same workpiece. Process parameters and feedstock used during spraying in booth #3 were undifferentiated over the repetitions, resulting in more uniform emission patterns.

3.2 Modal analysis of particle emissions

The recorded particle size distribution measurements were split in three modes: $\text{Mode}_{10\text{-}25\text{nm}}$ (particles with diameters from 10 to 25 nm), $\text{Mode}_{26\text{-}90\text{nm}}$ (particles with diameters from 26 to 90 nm:) and $\text{Mode}_{91\text{-}660\text{nm}}$ (particles from 91 to 660 nm), following the approach applied elsewhere (Salmatonidis et al., 2019). The algorithm for modal analysis uses a non-linear least square fitting, based on the interior-reflective Newton method (Coleman and Li, 1996, 1994). The three fitted lognormal curves and their parameters were calculated following the same assumptions and conditions suggested by Hussein et al. (2005). The NanoScan-SMPS measurements were expressed as $\mathrm{d}N/\mathrm{dLog}d_\mathrm{p}$ distributions before applying the modal analysis.

Figure 4a-c shows the modal analysis results for particles emitted inside booth #1. During the morning session (Figure 4a), $\text{Mode}_{26\text{-}90\text{nm}}$ was slightly more dominant compared to $\text{Mode}_{91\text{-}660\text{nm}}$, and together they comprised the majority of the emitted particles (94%). $\text{Mode}_{26\text{-}90\text{nm}}$ was dominant, accounting for 65% of the total particle number concentration, during the afternoon session (Figure 4c), while $\text{Mode}_{91\text{-}660\text{nm}}$ accounted for only 32% of the total particle number concentration. Their combined contribution still included the vast majority of the particles (97%), similarly to the morning session. The differences in the particle distributions recorded in the morning and in the afternoon sessions can be attributed to the different feedstock materials that

were used in each case. During the afternoon brake (i.e., no activities taking place in the workplace; cf. figure 4b) $Mode_{26\text{-}90nm}$ dominated as well the size distribution of particles but with significantly reduced number concentrations, in respect to plasma activity periods. In booth #3 (HVOF), the modal contributions are similar for the two different repetitions of the process (Figure 4d-e). $Mode_{26\text{-}90nm}$ was dominant accounting for 77 to 89% of the total particle number concentration, while the contribution of $Mode_{91\text{-}660nm}$ ranged from 16 to 8%. The contribution of $Mode_{10\text{-}25nm}$ (which includes particles formed by nucleation) was the lowest for all of the cases in terms of particle number emissions.

"Figure 4"

$Mode_{26\text{-}90nm}$ was dominant in both processes (APS and HVOF) for particles inside the spraying booths. Similar results were obtained in a previous work for particles transported from the booths to the worker area (Salmatonidis et al., 2019). These similarities are especially relevant from an exposure perspective, and show that the workers outside the booths wearing no personal protective equipment (PPE) were exposed to particles of similar sizes and chemical compositions as those operating inside the booths (where PPE was used).

3.3 Particle hygroscopicity and mixing state

Figures 5 and 6 show aggregated results of the measured hygroscopic factors of particles having dry electrical mobility diameters of 30 and 90 nm, respectively, during thermal spraying and as the HTDMA was sampling from within booth #1, #3 as well as outside booth #3. Particles were classified as hydrophobic/less hygroscopic (HP) having $g(87\%) \leq 1.15$, or as more hygroscopic (HS) with $g(87\%) > 1.15$. It should be noted that the threshold value of 1.15 is used here, following studies reporting hygroscopicity measurements from field observations (Swietlicki et al., 2008). The median values of the relative number fractions of HP or HS particles are in addition depicted in Figures 5 and 6, indicating the dominant mode (i.e., HP or HS). Time series of all hygroscopicity measurements are provided in SI (cf. Figures S4-S7). The hygroscopic factors $g(87\%)$ of the 90-nm particles during non-activity hours (i.e. background aerosols; cf. Figure S4) are clustered between 1.07 and 1.13 for the HP mode and at approximately 1.23 for the HS mode, being representative of urban background measurements (Swietlicki et al., 2008). During these periods, the sampled aerosol is externally mixed with HP particles being much more dominant. This is indicative of an area affected by both nearby and distant aerosol sources. The combination of the

low concentrations of 30-nm particles during non-working hours (Figure S5), together with the relatively increased particle losses inside the HTDMA, is responsible for the absence of the respective results during the non-activity periods (Figure S4). In contrast, during working hours, the signal of the HTDMA becomes strong when sampling 30-nm aerosols (cf. Figures S6 and S7), indicating a higher fraction of locally produced nano-scaled aerosol particles.

"Figure 5"

"Figure 6"

During non-activity periods (unshaded areas in Figures S6, S7), an externally mixed aerosol for ca. 45% of the cases for the 30-nm particles and ca. 76% for the 90-nm particles was observed. The lower occurrence of the externally mixed samples with 30-nm dry particles can be attributed to the fact that those are produced locally (i.e., in the workshop). As expected, freshly emitted particles, exhibited almost common hygroscopicities. During periods of spraying activities both the 30- and 90-nm particles exhibited a behavior indicating internally mixed particles, with the HP mode being dominant, as the median number fractions indicate (cf. bar plots in Figures 5 and 6). These cases should not be interpreted as a total absence of background aerosols but as a result of the significantly high process-generated nanoparticle emissions. These were up to 3 orders of magnitude higher when compared to the background and dominated the sample (cf. Figures 3a and 3b).

The most striking observation during the spraying activity periods was that the hygroscopic factor of the sampled aerosol particles was in many cases lower than unity, indicating that the particles undergo shape transformation within the HTDMA upon humidification, similarly to the observations of Tritscher et al. (2011) and Weingartner et al. (1995) made for irregularly shaped aerosols. This observation is much more pronounced for the 90-nm dry particles sampled by the HTDMA (i.e., median $g(87\%)$ values of HP mode < 1.0; cf. Figure 6), suggesting that their shape departs much more from that of a compact sphere compared to the 30-nm particles. Towards the end of the measurements, when the HTDMA was sampling outside booth #3 (i.e., central area) and the spraying system in that booth was operational (cf. Figures 5 and 6), the sampled aerosol was externally mixed, due to the dilution of process emitted particles (i.e., reducing their number concentrations), allowing the detection of background particles, as well. This was more pronounced for the 90-nm particles, which in all samples exhibited two hygroscopic modes, with

the first having $g(87\%)$ values < 1.0 (i.e., indicative of particles originating from the HVOF process), comprising ca. 60% of the total population. Aggregated results of the dynamic shape factors estimated for the particles emitted by both booths during thermal spraying are provided in Table 1.

"Table 1"

The hygroscopicity measurements showed that UFPs having dry electrical mobility diameters of 30 nm that are produced by the APS , exhibited on average some water uptake when exposed to 87% RH (i.e., less hygroscopic; cf. Figure 5). Upon inhalation, these particles will grow, due to the high RH in the human respiratory system (i.e., ca. 99% RH) by ca. 28%, reaching sizes of approx. 38.5 nm (cf. SI for the calculation). On the other hand, their 90-nm counterparts were characterized as hydrophobic, clearly exhibited irregular shapes and restructuring upon humidification (i.e., exhibiting hygroscopic factors with median values less than unity; cf. figure 6). Assuming that the 90-nm UFPs underwent a complete restructuring upon humidification, they will exhibit volume equivalent diameters of approx. 70 nm (i.e., having dynamic shape factors of 1.38; cf. Table 1). The 30-nm particles sampled from the HVOF exhibited in most of the cases some water uptake (i.e., less hygroscopic), while some of them exhibited hygroscopic growth factor values that were less than unity. On the other hand their 90-nm counterparts had hygroscopic factors less than unity in the majority of cases, suggesting that those were hydrophobic particles undergoing a restructuring upon humidification. Considering that the irregularly-shaped particles were completely restructured when humidified at 87% RH (i.e., operating RH of the HTDMA), we can assume that their volume equivalent diameters upon inhalation will be on average ca. 26 and 74 nm, for the 30- and 90- nm dry particles, respectively. It is expected that the deposition behavior of these UFPs inside the human respiratory tract will differ from those estimated if their hygroscopic behavior is not taken into account (i.e., by using only size distribution measurements, neglecting their hygroscopic restructuring). Although a detailed analysis of the deposition efficiencies of these particles in the human respiratory system is beyond the scope of this paper, the additional information on particle restructuring (i.e., size/shape change) upon humidification, which will also take place upon inhalation, can be therefore used for calculating their aerodynamic diameters more accurately (Hinds 1999).

Based on our results, the HTDMA can be used for distinguishing in-situ, thermal spraying process-generated UFPs, as their hygroscopic properties differ from those of background particles (i.e., significantly lower $g(87\%)$ values and shape change upon humidification). The ability of the HTDMA to distinguish the specific process-generated UFPs is not compromised by the existence of background aerosols as demonstrated by the measurements conducted outside booth #3 (HVOF), where both aerosol populations are identified (i.e., process-emitted and background UFPs; cf. Figure 6). In addition, based on the ability of the HTDMA to provide quantitative information on the particle number concentration fraction residing in each population (i.e., background vs. process-generated UFPs), it can be used to complement particle distribution measurements for calculating the number concentration of particles in each population. The above mentioned capabilities of the HTDMA allow the in situ and near-real-time identification of fugitive, process-generated UFPs. However, a limiting factor of existing HTDMA systems is their bulk size; despite that the HTDMA used in this work was mobile, a few days of sampling were needed for covering the whole area of the manufacturing workshop, under all conditions. It should be noted here that in contrast to other aerosol instrumentation used in exposure studies, the HTDMA is so far limited in conducted long-term, unattended atmospheric observations in static locations (i.e., urban and/or remote atmospheric stations), thus no need of reducing its dimensions and increasing its portability exist. Future works should address the need of a highly mobile, portable HTDMA, for use in exposure studies, in order to address the above mentioned limitation.

3.3 TEM analysis

TEM images of particles collected inside booth #1 are shown in Figure 7a-b. Chain fractal-like particles with different sizes and numbers of primary particles were observed across the TEM grid. As a result, only the size of the primary particles forming the fractal-like particles can be obtained. Spherical or spheroid shape of primary particles, ranging from 5 to 20 nm, can be observed in the TEM images of fractal-like particles produced in booth #1 (Figure 7a-b), and their composition was found to be similar to the feedstock material (cf. Figure S8a). TEM images of particles sampled inside booth #3 during spraying are shown in Figure 7c-d. Irregularly-shaped primary particles appear to be strongly bonded, indicating that they have undergone mild sintering, and therefore it becomes challenging to distinguish them even in the higher TEM magnification (Figure 7d). This could also be an indication that these irregularly-shaped particles have formed by

agglomeration through high energy collisions due hypersonic impactions. The chemical composition of the particles emitted was similar to that of the micron-sized feedstock used (Figure S8b); confirming that thermal spraying was their source.

"Figure 7"

4. Conclusions

High concentrations of process-generated ultrafine particles (UFPs), which were often higher than 10^6 cm^{-3}, were monitored at an industrial workplace setting during thermal spraying inside the spraying booths of the studied facility. Emission patterns were irregular in the case of the Atmospheric Plasma Spraying (APS) and more uniform during High Velocity Oxy-Fuel (HVOF). Modal analysis of the emissions showed that the majority of the emitted UFPs were in the size range of 20 to 100 nm, regardless of the process and the operating conditions. Particles were emitted inside the spraying booths where workers were equipped with respiratory protective equipment, but they also impacted the area where workers were not equipped with respiratory protective equipment.

Measurements of the hygroscopicity and mixing state of the sampled aerosol were also carried out for providing complementary information on the UFP in the breathing air in the facility, as well as a means to distinguish between process-generated and background aerosols. Particles originating from thermal spraying that had a size of 30 nm exhibited hygroscopicities which did not differ significantly from other aerosol particles sampled when thermal spraying was not operational. However, taking into account that 30-nm particles were observed by the HTDMA only during working hours, their presence has to be attributed to processes taking place inside the workshop. The shape of these particles was closer to that of a sphere, while based on their measured hygroscopicities they are expected to grow in size by ca. 28% upon inhalation (i.e., at 99% RH). On the other hand, 90-nm process-generated particles were hydrophobic at 87% RH and underwent a more significant shrinkage upon humidification (i.e., exhibiting hygroscopic growth factors that were less than unity). This allowed to clearly distinguish them from other particles of the same dry size that were present in the workplace. In addition, it is expected that the deposition efficiencies of the 90-nm irregularly shaped particles in the human respiratory system, will be different than that estimated when not accounting for their restructuring (i.e., based only in electrical mobility measurements of their size and assuming spherical particles), as their size and shape will change

upon inhalation (i.e., ca. 99% RH). The additional information provided by the HTDMA can complement existing methods used for an accurate assessment of the health effects associated to process-generated UFPs. Changes in their size and shape upon inhalation can impact on other properties, such as their lung deposition surface area, while changing their deposition patterns inside the human respiratory system. This information underlines the importance of including hygroscopicity measurements on exposure studies, and motivates the need of increasing the portability of HTDMAs to facilitate their employment in workplaces.

TEM/EDX analysis showed that fractal-like particles were dominant in samples collected from both processes at dry conditions, exhibiting different shapes and sizes, thereby, validating the HTDMA observations. This analysis also confirmed that process-generated aerosols had the same composition as the feedstock material, verifying that thermal spraying (APS, HVOF) was the dominant UFP source in the breathing air at the facility.

Acknowledgements

The authors kindly acknowledge TM COMAS (http://www.tmcomas.com) for their committed cooperation. The current work was carried out in the framework of the CERASAFE project (www.cerasafe.eu), with the support of SIINN ERA-NET (project id: 16), and was funded by the Spanish MINECO (PCIN-2015-173-C02-01) and the respective French agency (Region Hauts de France). Partial funding from the “Generalitat de Catalunya” (project number: AGAUR 2017 SGR41) is also acknowledged.

References

Agarwal, J.K., Sem, G.J., 1980. Continuous flow, single-particle-counting condensation nucleus counter. J. Aerosol Sci. 11, 343–357. https://doi.org/https://doi.org/10.1016/0021-8502(80)90042-7

Anselm, A., Heibel, T., Gebhart, J., Ferron, G., Inhalation, P., 1990. of Sodium Chloride Particles in the Human Respiratory Tract. Growth Factors 21, 427–430.

Asbach, C., Alexander, C., Clavaguera, S., Dahmann, D., Dozol, H., Faure, B., Fierz, M., Fontana, L., Iavicoli, I., Kaminski, H., MacCalman, L., Meyer-Plath, A., Simonow, B., van Tongeren, M., Todea, A.M., 2017. Review of measurement techniques and methods for assessing personal exposure to airborne nanomaterials in workplaces. Sci. Total Environ. 603–604, 793–806. https://doi.org/10.1016/j.scitotenv.2017.03.049

Asbach, C., Clavaguera, S., Todea, A.M., 2016. Measurement Methods for Nanoparticles in Indoor and Outdoor Air, in: Viana, M. (Ed.), Indoor and Outdoor Nanoparticles: Determinants of Release and Exposure Scenarios. Springer International Publishing, Cham, pp. 19–49. https://doi.org/10.1007/698_2015_423

Asbach, C., Kuhlbusch, T. a J., Kaminski, H., Plitzko, S., Götz, U., Voetz, M., Dahmann, D., 2012. Authors : SOP-Tiered Approach Tiered Approach for the assessment of exposure to airborne nanoobjects in work- places.

Bezantakos, S., Barmpounis, K., Giamarelou, M., Bossioli, E., Tombrou, M., Mihalopoulos, N., Eleftheriadis, K., Kalogiros, J., Allan, J.D., Bacak, A., Percival, C.J., Coe, H., Biskos, G., 2013. Chemical composition and hygroscopic properties of aerosol particles over the Aegean Sea. Atmos. Chem. Phys. 13, 11595–11608. https://doi.org/10.5194/acp-13-11595-2013

Bezantakos, S., Huang, L., Barmpounis, K., Martin, S. T. and Biskos G., 2016. Relative humidity non-uniformities in hygroscopic tandem differential mobility analyzer measurements. J. Aerosol Sci., 101, 1-9.

Biskos, G., Russell, L.M., Buseck, P.R., Martin, S.T., 2006a. Nanosize effect on the hygroscopic growth factor of aerosol particles. Geophys. Res. Lett. 33, 2–5. https://doi.org/10.1029/2005GL025199

Biskos, G., Russell, L. M., Buseck, P. R. and Martin S. T., 2006b. Prompt deliquescence and efflorecence of aerosol nanoparticles. Atmos. Chem. Phys., 6, 4633-4642

Ching, J., Kajino, M., 2018. Aerosol mixing state matters for particles deposition in human respiratory system. Sci. Rep. 8, 8864. https://doi.org/10.1038/s41598-018-27156-z

Coleman, T.F., Li, Y., 1996. An Interior Trust Region Approach for Nonlinear Minimization Subject to Bounds. SIAM J. Optim. 6, 418–445. https://doi.org/10.1137/0806023

Coleman, T.F., Li, Y., 1994. On the convergence of interior-reflective Newton methods for nonlinear minimization subject to bounds. Math. Program. 67, 189–224. https://doi.org/10.1007/BF01582221

Dahmann, D., 2016. Exposure Assessment: Methods, in: Viana, M. (Ed.), Indoor and Outdoor Nanoparticles: Determinants of Release and Exposure Scenarios. Springer International Publishing, Cham, pp. 51–72. https://doi.org/10.1007/698_2015_436

Fauchais, P., Vardelle, A., Dussoubs, B., 2001. Quo Vadis thermal spraying? J. Therm. Spray Technol. 10, 44–66. https://doi.org/10.1361/105996301770349510

Ferron, G.A., Kreyling, W.G., Haider, B., 1988. AND DEPOSITION IN THE H U M A N RESPIRATORY TRACT * Ioo [19, 611–631.

Fonseca, A.S., Maragkidou, A., Viana, M., Querol, X., Hämeri, K., de Francisco, I., Estepa, C., Borrell, C., Lennikov, V., de la Fuente, G.F., 2016. Process-generated nanoparticles from ceramic tile sintering: Emissions, exposure and environmental release. Sci. Total Environ. 565, 922–932. https://doi.org/10.1016/j.scitotenv.2016.01.106

Fonseca, A.S., Viana, M., Querol, X., Moreno, N., de Francisco, I., Estepa, C., de la Fuente, G.F., 2015. Ultrafine and nanoparticle formation and emission mechanisms during laser processing of ceramic materials. J. Aerosol Sci. 88, 48–57. https://doi.org/10.1016/j.jaerosci.2015.05.013

Gakidou, E., Afshin, A., Abajobir, A.A., et Al., A., 2017. Global, regional, and national comparative risk assessment of 84 behavioural, environmental and occupational, and metabolic risks or clusters of risks, 1990–2016: a systematic analysis for the Global Burden of Disease Study 2016. Lancet 390, 1345–1422. https://doi.org/10.1016/S0140-6736(17)32366-8

Ganguly, P., Breen, A., Pillai, S.C., 2018. Toxicity of Nanomaterials: Exposure, Pathways, Assessment, and Recent Advances. ACS Biomater. Sci. Eng. acsbiomaterials.8b00068. https://doi.org/10.1021/acsbiomaterials.8b00068

Hussein, T., Maso, M., Petäjä, T., Koponen, I., Paatero, P., Aalto, P., Hämeri, K., Kulmala, M., 2005. Evaluation of an automatic algorithm for fitting the particle number size distributions. Boreal Environ. Res. 10, 337–355.

Kalantzi, O., Biskos G., 2014. Methods for assessing basic particle properties and cytotoxicity of engineered nanaparticles. Toxics 2 (1), 79-91.

Kelesidis, G.A., Furrer, F.M., Wegner, K., Pratsinis, S.E., 2018. Impact of Humidity on Silica Nanoparticle Agglomerate Morphology and Size Distribution. Langmuir 34, 8532–8541. https://doi.org/10.1021/acs.langmuir.8b00576

Knutson, E.O., Whitby, K.T., 1975. Aerosol classification by electric mobility: apparatus, theory, and applications. J. Aerosol Sci. 6, 443–451. https://doi.org/10.1016/0021-8502(75)90060-9

Krämer, L., Pöschl, U., Niessner, R., 2000. Microstructural rearrangement of sodium chloride condensation aerosol particles on interaction with water vapor. J. Aerosol Sci. 31, 673–685. https://doi.org/10.1016/S0021-8502(99)00551-0

Kuhlbusch, T.A.J., Asbach, C., Fissan, H., Göhler, D., Stintz, M., 2011. Nanoparticle exposure at nanotechnology workplaces: A review. Part. Fibre Toxicol. 8, 1–18. https://doi.org/10.1186/1743-8977-8-22

Kuhlbusch, T.A.J., John, A.C., Quass, U., 2009. Sources and source contributions to fine particles. Biomarkers 14, 23–28. https://doi.org/10.1080/13547500902965377

Landrigan, P.J., 2017. Air pollution and health. Lancet Public Heal. 2, e4–e5. https://doi.org/10.1016/S2468-2667(16)30023-8

Li, C.-J., Wang, Y.-Y., Yang, G.-J., Ohmori, A., Khor, K.A., 2004. Effect of solid carbide particle size on deposition behaviour, microstructure and wear performance of HVOF cermet coatings. Mater. Sci. Technol. 20, 1087–1096. https://doi.org/10.1179/026708304225019722

Li, M., Christofides, P.D., 2006. Computational study of particle in-flight behavior in the HVOF thermal spray process. Chem. Eng. Sci. 61, 6540–6552. https://doi.org/10.1016/j.ces.2006.05.050

Limbach, L.K., Wick, P., Manser, P., Grass, R.N., Bruinink, A., Stark, W.J., 2007. Exposure of Engineered Nanoparticles to Human Lung Epithelial Cells: Influence of Chemical Composition and Catalytic Activity on Oxidative Stress. Environ. Sci. Technol. 41, 4158–4163. https://doi.org/10.1021/es062629t

Löndahl, J., Massling, A., Pagels, J., Swietlicki, E., Vaclavik, E., Loft, S., 2007. Size-Resolved Respiratory-Tract Deposition of Fine and Ultrafine Hydrophobic and Hygroscopic Aerosol Particles During Rest and Exercise. Inhal. Toxicol. 19, 109–116. https://doi.org/10.1080/08958370601051677

Marick M. M., 2008. Bipolar Diffusion Charging of Soot Aggregates. Aerosol Sci. Technol. 42, 247-254.

Mauer, G., Vaen, R., Stöver, D., 2011. Plasma and particle temperature measurements in thermal spray:

Approaches and applications. J. Therm. Spray Technol. 20, 391–406. https://doi.org/10.1007/s11666-010-9603-z

McMurry, P.H., Stolzenburg, M.R., 1989. On the sensitivity of particle size to relative humidity for Los Angeles aerosols. Atmos. Environ. 23, 497–507. https://doi.org/10.1016/0004-6981(89)90593-3

Oberdörster, G., 2001. Pulmonary effects of inhaled ultrafine particles. Int. Arch. Occup. Environ. Health 74, 1–8. https://doi.org/10.1007/s004200000185

OECD, 2015. Harmonized Tiered Approach to Measure and Assess the Potential Exposure to Airborne Emissions of Engineered Nano-Objects and their Agglomerates and Aggregates at Workplaces. Ser. Saf. Manuf. Nanomater. No.55 55, JT03378848-JT03378848.

Ono-Ogasawara, M., Serita, F., Takaya, M., 2009. Distinguishing nanomaterial particles from background airborne particulate matter for quantitative exposure assessment. J. Nanoparticle Res. 11, 1651–1659. https://doi.org/10.1007/s11051-009-9703-1

Pawlowski, L., 2008. The Science and Engineering of Thermal Spray Coatings, The Science and Engineering of Thermal Spray Coatings: Second Edition. https://doi.org/10.1002/9780470754085

Peters, T.M., Elzey, S., Johnson, R., Park, H., Grassian, V.H., Maher, T., O'Shaughnessy, P., 2009. Airborne monitoring to distinguish engineered nanomaterials from incidental particles for environmental health and safety. J. Occup. Environ. Hyg. 6, 73–81. https://doi.org/10.1080/15459620802590058

Pietroiusti, A., Stockmann-Juvala, H., Lucaroni, F., Savolainen, K., 2018. Nanomaterial exposure, toxicity, and impact on human health. Wiley Interdiscip. Rev. Nanomedicine Nanobiotechnology 1–21. https://doi.org/10.1002/wnan.1513

Planche, M.P., Bolot, R., Coddet, C., 2003. In-Flight Characteristics of Plasma Sprayed Alumina Particles : Measurements , Modeling , and Comparison 12, 101–111.

Rader, D.J., McMurry, P.H., 1986. Application of the tandem differential mobility analyzer to studies of droplet growth or evaporation. J. Aerosol Sci. 17, 771–787. https://doi.org/10.1016/0021-8502(86)90031-5

Salmatonidis, A., Ribalta, C., Sanfélix, V., Bezantakos, S., Biskos, G., Vulpoi, A., Simion, S., Monfort, E., Viana, M., 2019. Workplace Exposure to Nanoparticles during Thermal Spraying of Ceramic Coatings. Ann. Work Expo. Heal. 63, 91–106. https://doi.org/10.1093/annweh/wxy094

Salmatonidis, A., Viana, M., Pérez, N., Alastuey, A., de la Fuente, G.F., Angurel, L.A., Sanfélix, V., Monfort, E., 2018. Nanoparticle formation and emission during laser ablation of ceramic tiles. J. Aerosol Sci. 126, 152–168. https://doi.org/10.1016/j.jaerosci.2018.09.006

Schill, A.L., Chosewood, L.C., 2013. The NIOSH total worker health program: An overview. J. Occup. Environ. Med. 55, 10–13. https://doi.org/10.1097/JOM.0000000000000037

Song, Y., Li, X., Du, X., 2009. Exposure to nanoparticles is related to pleural effusion, pulmonary fibrosis and granuloma. Eur. Respir. J. 34, 559–567. https://doi.org/10.1183/09031936.00178308

Swietlicki, E., Hansson, H.C., Hämeri, K., Svenningsson, B., Massling, A., Mcfiggans, G., Mcmurry, P.H., Petäjä, T., Tunved, P., Gysel, M., Topping, D., Weingartner, E., Baltensperger, U., Rissler, J., Wiedensohler, A., Kulmala, M., 2008. Hygroscopic properties of submicrometer atmospheric aerosol particles measured with H-TDMA instruments in various environments - A review. Tellus, Ser. B Chem. Phys. Meteorol. 60 B, 432–469. https://doi.org/10.1111/j.1600-0889.2008.00350.x

Tritscher, T., Jurnyi, Z., Martin, M., Chirico, R., Gysel, M., Heringa, M.F., Decarlo, P.F., Sierau, B., Prévt, A.S.H., Weingartner, E., Baltensperger, U., 2011. Changes of hygroscopicity and morphology during ageing of diesel soot. Environ. Res. Lett. 6. https://doi.org/10.1088/1748-9326/6/3/034026

van Broekhuizen, P., 2017. Applicability of provisional NRVs to PGNPs and FCNPs Applicability of provisional NRVs to PGNPs and FCNPs. Amsterdam. https://doi.org/10.13140/RG.2.2.18241.25445

Voliotis, A., Bezantakos, S., Giamarelou, M., Valenti, M., Kumar, P., Biskos, G., 2014. Nanoparticle emissions from traditional pottery manufacturing. Environ. Sci. Process. Impacts 16, 1489–1494. https://doi.org/10.1039/C3EM00709J

Weingartner, E., Baltensperger, U., Burtscher, H., 1995. Growth and Structural Change of Combustion Aerosols at High Relative Humidity. Environ. Sci. Technol. 29, 2982–2986. https://doi.org/10.1021/es00012a014

World Health Organization, 2016. Ambient Air Pollution: A global assessment of exposure and burden of disease. World Heal. Organ. 1–131. https://doi.org/9789241511353

Zhang, M., Jian, L., Bin, P., Xing, M., Lou, J., Cong, L., Zou, H., 2013. Workplace exposure to nanoparticles from gas metal arc welding process. J. Nanoparticle Res. 15. https://doi.org/10.1007/s11051-013-2016-4

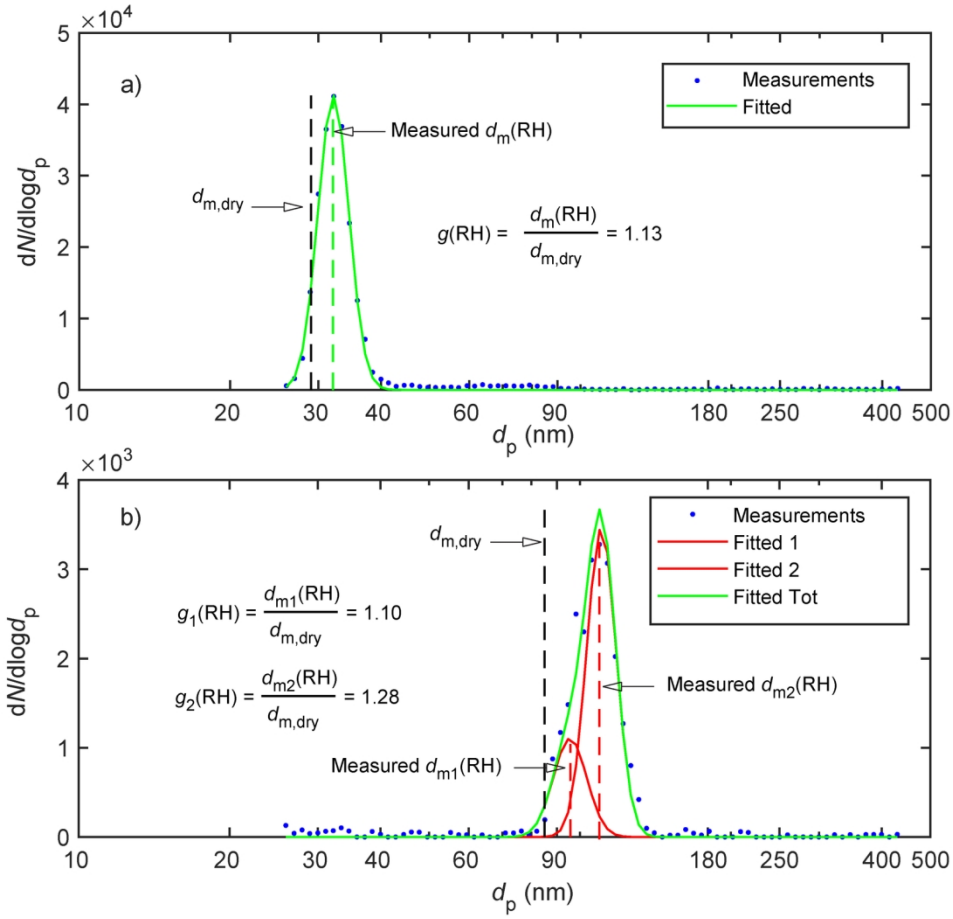

Figure 1. Example of inverted HTDMA measurements of particles having dry electrical mobility diameters of 30 (a) and 90 (b) nm, and their corresponding hygroscopic factor(s) at 87% RH, taken from within booth #3 when the door was open and no activity was taking place. Note that in the 30-nm particles were internally mixed (i.e., unimodal distribution when exposed to 87% RH), while in contrast their 90-nm counterparts exhibited a wider distribution upon humidification in these measurements. This can be analyzed in two separate modes (indicating that they were externally mixed), thus having two hygroscopic factors (i.e., g_1 and g_2).

150x142mm (300 x 300 DPI)

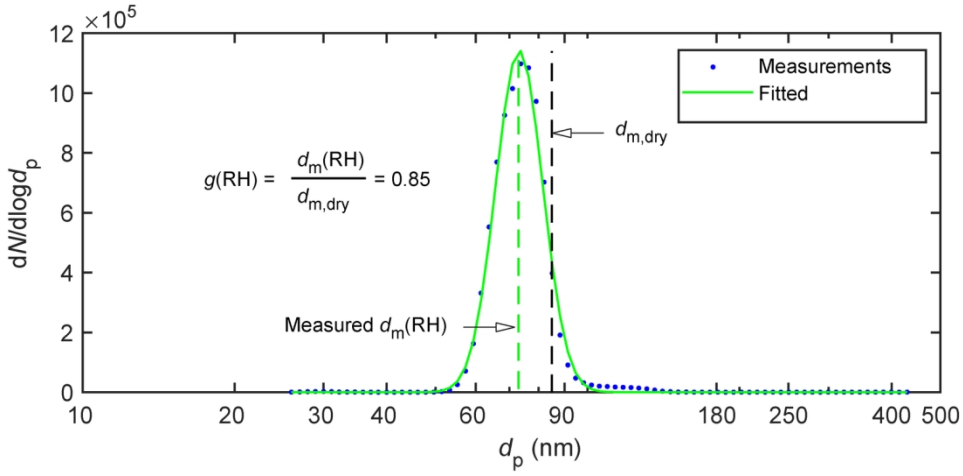

Figure 2. Example of an inverted HTDMA measurement of particles having a dry electrical mobility diameter of 90 nm, and their corresponding hygroscopic factor at 87% RH, taken from within plasma #3 booth during thermal spraying. Note that in these measurements, the assumed 90-nm particles (i.e., based on the operational settings of DMA-1, corresponding for spherical particles) exhibited a unimodal distribution (i.e., internally mixed) when exposed to 87% RH, with a hygroscopic factor < 1.0. The latter is a clear indication of hydrophobic particles with irregular shape, that undergo restructuring upon humidification at 87% RH.

149x72mm (300 x 300 DPI)

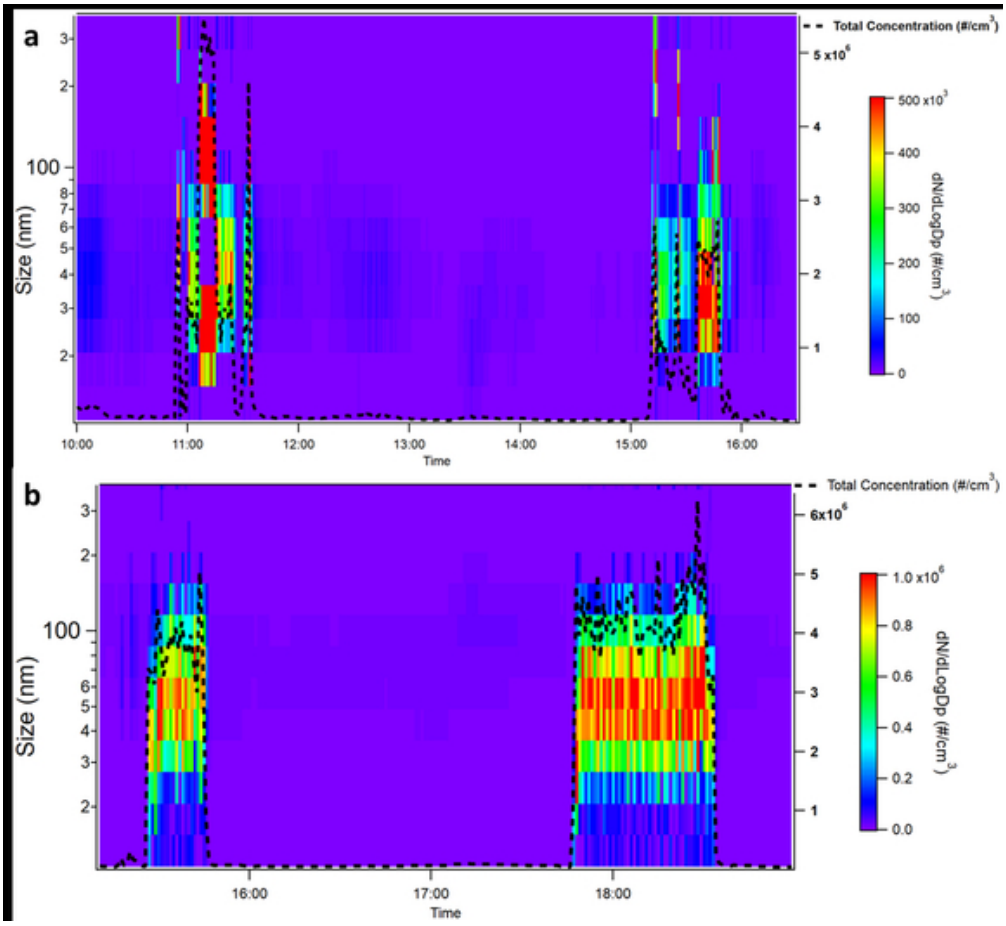

Figure 3. Evolution of the particle number size distributions: a) inside booth #1 (APS) and b) inside booth #3 (HVOF). Total particle number concentrations (dashed black curve) and the corresponding size distributions (NanoScan-SMPS) are shown for both processes.

48x44mm (300 x 300 DPI)

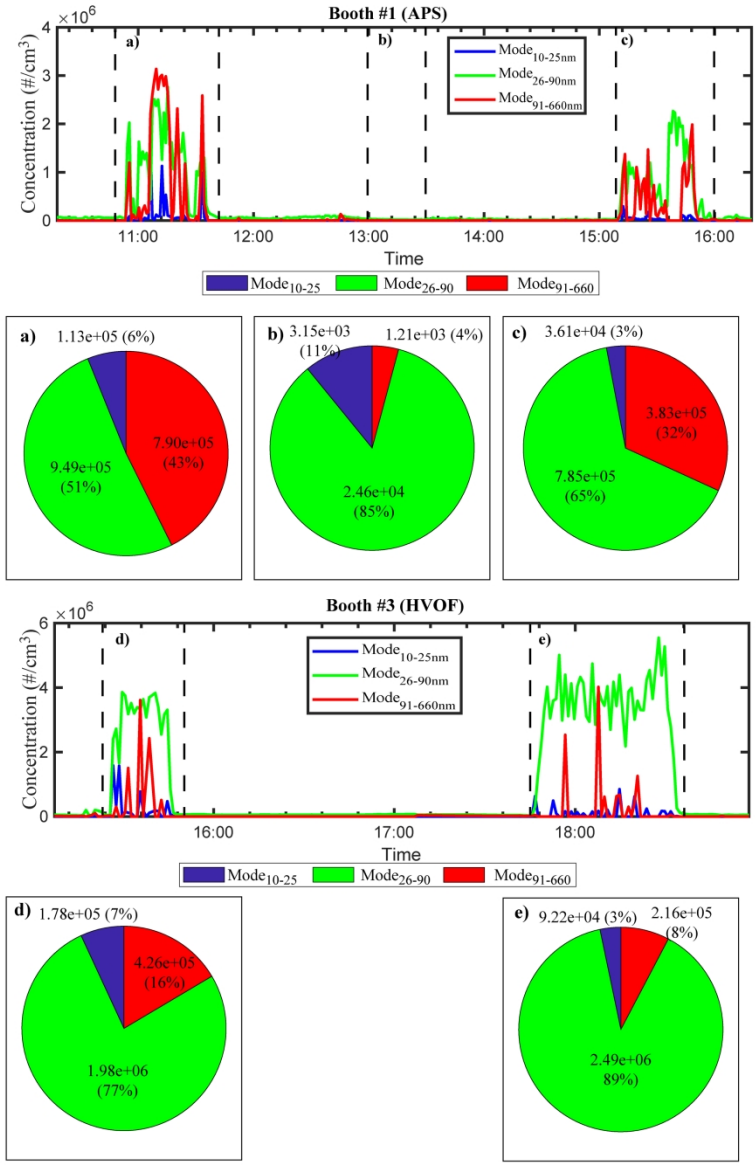

Figure 4. Modal analysis results for particles emitted inside booth #1 (a-c) and inside booth #3 (d, e). The time intervals (a, c and d, e) represent different repetitions of each thermal spraying process, while in contrast the afternoon break (i.e., no activity period) is marked with the time interval (b). The numbers in the pie plots depict the average number concentration of each mode (in #/cm^3), while the percentages (i.e., in parenthesis) provide the average fraction of the number concentration of each mode in respect to the total number concentration of particles.

199x310mm (300 x 300 DPI)

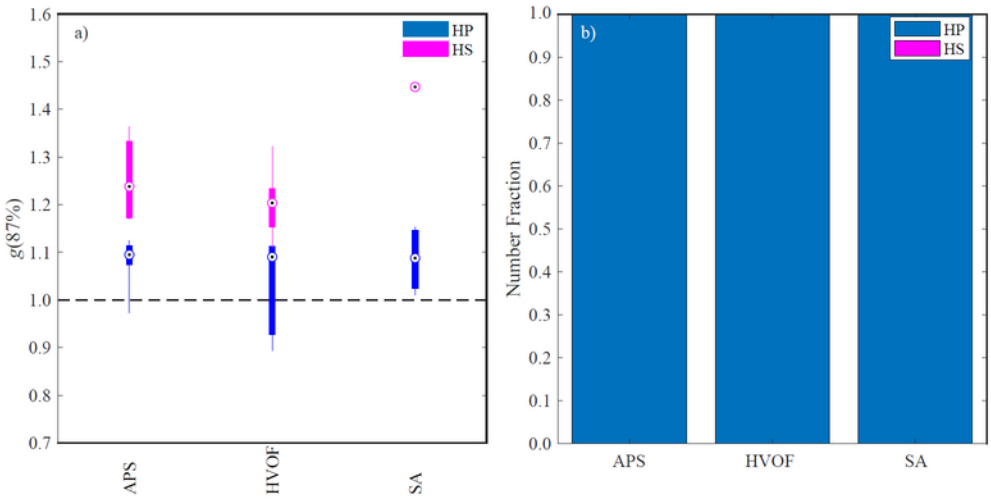

Figure 5. Aggregated hygroscopic factor measurements (a) and median values of the relative number fraction of each hygroscopic mode (b) of particles sampled with the HTDMA having electrical mobility diameters of 30 nm when the plasma processes in booth #1 (APS) and booth #3 (HVOF) were active. Results are also shown when booth #3 was active but the HTDMA sampled from the storage area outside booth #3 (SA). Particles exhibiting hygroscopic factors below 1.15 (hydrophobic/less hygroscopic; HP) are denoted with different color (i.e. blue), than the more hygroscopic ones (i.e., hygroscopic factor > 1.15; HS). The dotted circles denote the median values of the each hygroscopic mode, whereas the range and 25th, 75th percentiles are depicted with narrow and wide solid lines, respectively.

66x33mm (300 x 300 DPI)

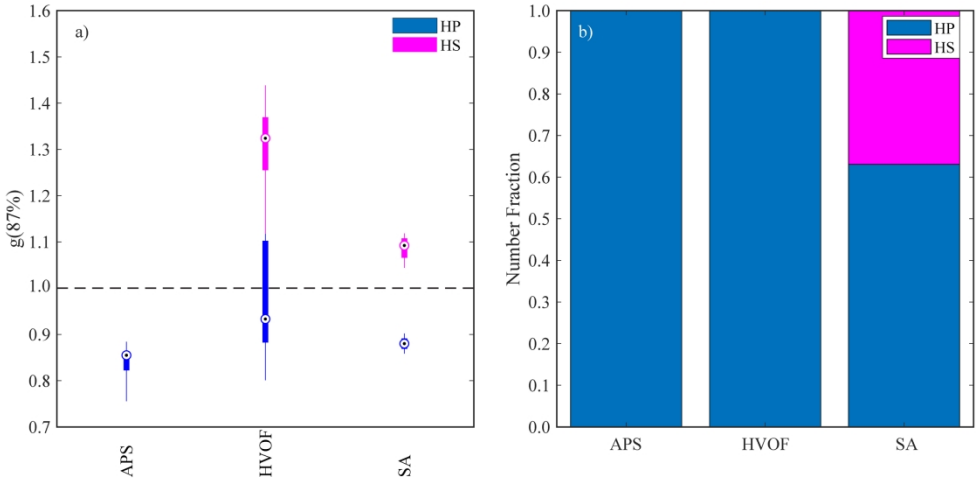

Figure 6. Aggregated hygroscopic factor measurements (a) and median values of the relative number fraction of each hygroscopic mode (b) of particles sampled with the HTDMA having electrical mobility diameters of 90-nm when the plasma processes in booth #1 (APS) and booth #3 (HVOF) were active. Results are also shown when booth #3 was active but the HTDMA sampled from the storage area outside booth #3 (SA). Particles exhibiting hygroscopic factors below 1.15 (hydrophobic/less hygroscopic; HP) are denoted with different color (i.e. blue), than the more hygroscopic ones (i.e., hygroscopic factor > 1.15; HS). The dotted circles denote the median values of the each hygroscopic mode, whereas the range and 25th, 75th percentiles are depicted with narrow and wide solid lines, respectively.

239x122mm (300 x 300 DPI)

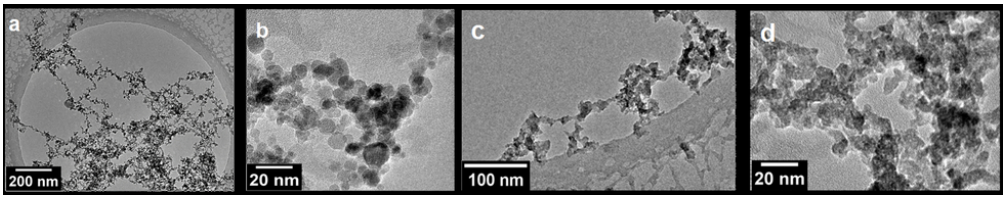

Figure 7. TEM images of the particles emitted during APS in booth #1 (a, b), and during HVOF in booth #3 (c-d).

82x15mm (300 x 300 DPI)

Tables

Table 1. Results showing the average and standard deviation (where applicable) of the estimated dynamic shape factor χ of the irregularly-shaped particles (i.e., $g(87\%)<1.0$).

Booth	$d_{m,dry}$ (nm)	χ
#1	30	1.05*
#1	90	1.38 ± 0.16
#3	30	1.20 ± 0.08
#3	90	1.28 ± 0.12

* No standard deviation is provided as only one sample exhibiting a value of $g(87\%)<1.0$ was observed.

Supplemental Information

Particle size distributions and hygroscopic restructuring of ultrafine particles emitted during thermal spraying

A. Salmatonidis[1,2], M. Viana[1], G. Biskos[3,4], S. Bezantakos[3,5]*

**Corresponding author: S. Bezantakos*

[1]*Institute of Environmental Assessment and Water Research (IDAEA-CSIC), Barcelona, Spain*

[2]*Department of Chemical Engineering and Analytical Chemistry, Faculty of Chemistry, University of Barcelona*

[3]*Energy Environment and Water Research Centre, The Cyprus Institute, Nicosia, Cyprus*

[4]*Faculty of Civil Engineering and Geosciences, Delft University of Technology, Delft, The Netherlands*

[5]*Université du Littoral Côte d' 'Opale, Dunkerque, France*

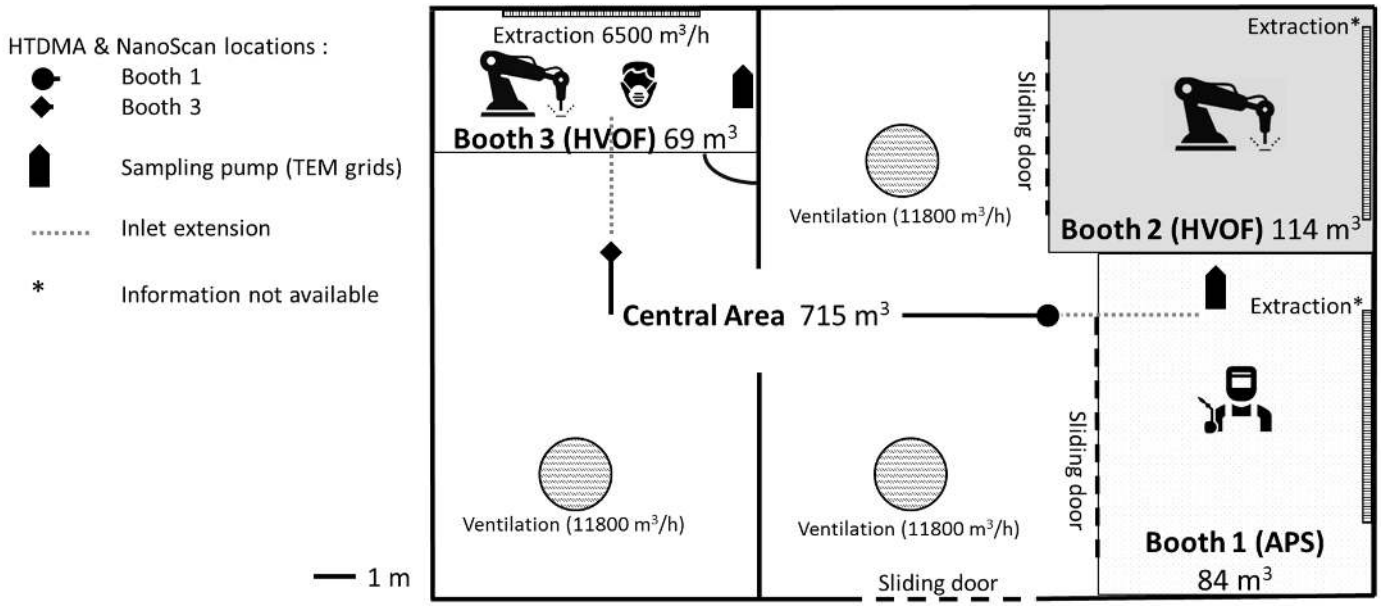

Figure S1. Schematic illustration or the facility investigated

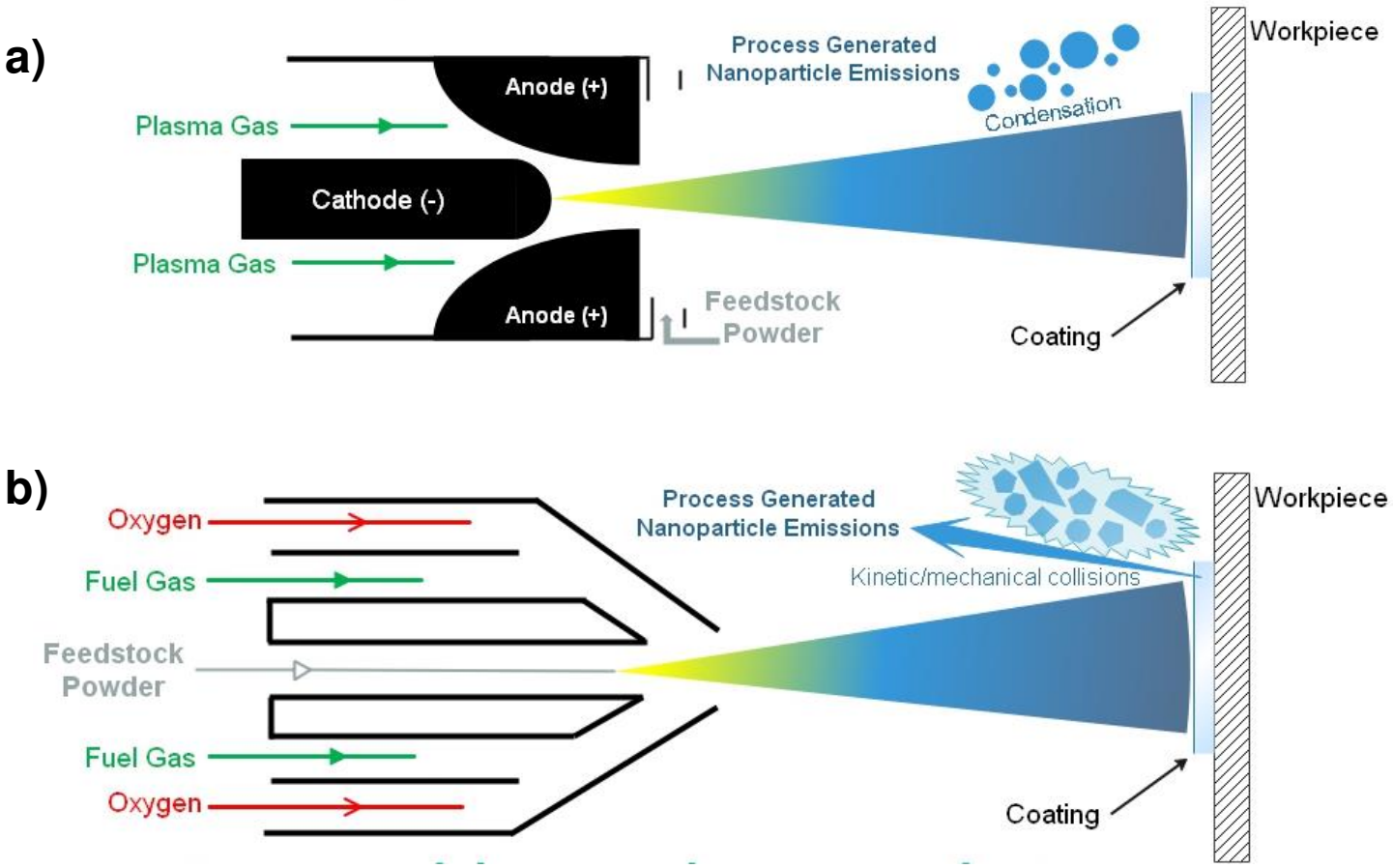

Figure S2. Schematic illustration of the thermal spraying techniques, (a) APS and (b) HVOF and their potential particle emission mechanisms.

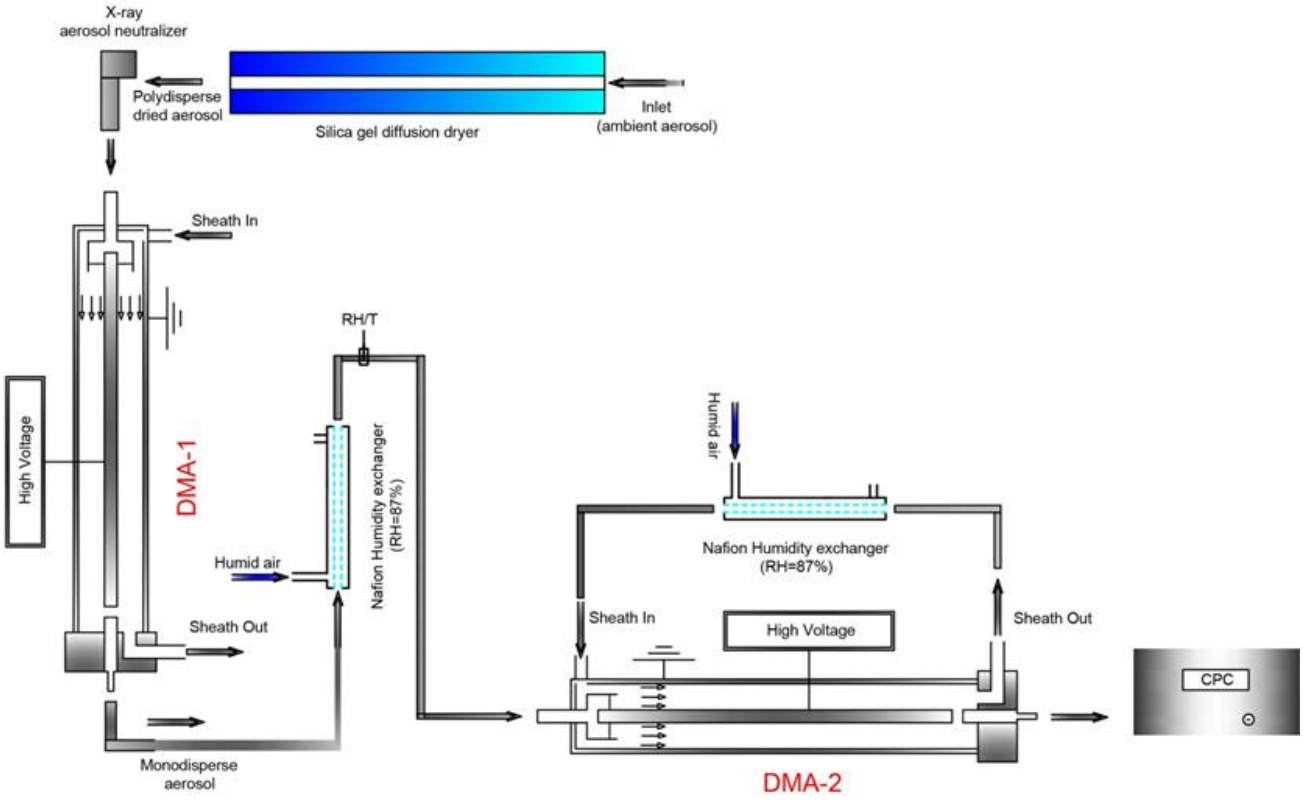

Figure S3. Major parts of the HTDMA system assembled for the characterization of UFPs hygroscopicity and mixing state.

Sampled particles were initially dried through a silica gel diffusion drier, brought to a charge equilibrium by passing through a soft X-ray aerosol neutralizer (TSI Model 3088) before entering the first DMA of the system (DMA-1). The quasi-monodisperse particles downstream DMA-1 are then exposed to elevated RH conditions by passing through a nafion membrane humidity exchanger (Permapure Model MD-700-06S-1), before their size distribution is measured by the second DMA (DMA-2) of the system that is coupled to a CPC (TSI 3010). Both DMAs employ closed loop sheath flows, while an additional humidification system, consisting of a second nafion humidifier (Permapure PD-50T-MPR) is added to the sheath flow of DMA-2 in order to maintain it at the same RH level with that of the sample flow. Two RH and temperature sensors (Rotronic HC02-05), together with a software closed loop control (National Instruments Labview 2014), are utilized for measuring and controlling the stability of the RHs in the system. The system was operated at a constant 87±2% RH, as this is above the deliquescence RH (i.e., RH above which a solid particle will form a droplet) of ammonium sulfate (i.e., one of the most abundant, hygroscopic, inorganic species in the atmosphere), while being low enough to

prevent accidental forming of supersaturated conditions in parts of the HTDMA. The performance of the HTDMA was tested prior the measuring campaign by using ammonium sulfate particles, which have known and well studied hygroscopic properties (i.e., well defined deliquescence RH, and hygroscopic growth factors at different RH).

Deriving hygroscopic factor from the HTDMA.

In the HTDMA the first DMA (DMA-1) operates at a steady voltage during each sample, thus constantly classifying particles having a quasi monodisperse electrical mobility (*Z*), while the voltage of DMA-2 is scanned, allowing the classification of particles having different electrical mobilities, which are then detected by the CPC. In general, the electrical mobility *Z* of the particles that are classified in a cylindrical DMA (i.e., like the ones used in the HTDMA) is related with its geometrical features and operating conditions (Baron and Willeke, 2001) as:

$$Z = \frac{(Q_{\mathrm{sh}} + Q_{\mathrm{e}}) \ln \frac{R_2}{R_1}}{4\pi V L}. \quad \text{(S1)}$$

Here, R_1, R_2 are respectively the inner and outer radii of the DMA, *L* is characteristic classification length, Q_{sh} the sheath flow rate, Q_{e} the excess flow rate and *V* the applied potential in its inner electrode.

In the case of spherical particles, *Z* is related to particle diameter (*d*) using Hinds (1999):

$$Z = \frac{neCc}{3\pi\mu d}, \quad \text{(S2)}$$

where *n* is the number of elementary charges, *e* the electron charge (1.6e-19 Cb), *μ* the air viscosity (1.81e-5 Pa S, at 20 ˚C) and *Cc* the Cunningham slip correction factor.

The Cunningham slip correction factor, *Cc*, can be calculated via the empirical formula (Allen and Raabe, 1985) as:

$$Cc(Kn) = 1 + Kn\left[a + b\exp\left(-\frac{c}{Kn}\right)\right]. \quad \text{(S3)}$$

Here *Kn* is the Knudsen number, which is the ratio of the gas mean free path (*λ*) to the radius of the spherical particle (*r*), while *a*= 1.257, *b*=0.4, *c*=1.1, are fitted parameters (Davies, 1945). Note that the *Kn* number, calculated as $Kn = 2\lambda/d$, where λ is the gas mean free path and *d* the diameter of particles, is used for defining the behavior of a particle while moving inside its surrounding gas molecules (i.e., its flow regime). For example, a particle much bigger than the gas mean free path (i.e, $Kn \ll 1$) will be subjected to a number of gas molecules collisions while

a particle, much smaller than the gas mean free path (i.e., $Kn>>1$) will be subjected to significantly lower collisions by the surrounding gas molecules (i.e., resulting in a reduction in its drag).

Assuming particles of spherical shape, carrying one elementary charge, equations S1 to S3 are used for inverting the HTDMA measurements and for calculating the geometric mean electrical mobility diameters of particles selected by DMA-1 and measured by DMA-2 and the CPC, thus deriving their hygroscopic factor.

Calculating particle hygroscopic factor on different than 87% RH.

The water affinity of soluble particulate matter can be represented by the single hygroscopic parameter κ (Petters and Kreidenweis, 2007), which can be also used for calculating its water uptake characteristics at various RHs. The value of κ can be calculated from the measured (i.e., by the HTDMA) hygroscopic factor (Kreidenweis et al., 2008):

$$\kappa_{HTDMA} = \frac{\left(g(87\%)^3 - 1\right)}{a_w/(1-a_w)}\ , \tag{S4}$$

where $g(87\%)$ is the measured hygroscopic factor (i.e., at 87% RH in our measurements) and a_w is the water activity of the solution droplet, which can be calculated by:

$$a_w \approx \frac{\mathrm{RH}}{100}\left(exp\left(\frac{4\sigma_{s/\alpha}\ M_w}{RT\rho_w d_m(\mathrm{RH})}\right)\right)^{-1}. \tag{S5}$$

Here $\sigma_{s/a}$ and M_w are the surface tension and molecular weight of pure water (0.072 J m^{-2} and 18^{-3} kg/mol, respectively), R is the universal gas constant, T is the absolute temperature, ρ_w is the density of water and d_m is the diameter of the particles at 87% RH.

The single hygroscopic parameter κ (i.e., calculated using the Eqs. S4 and S5) can be used for predicting the hygroscopic factor of the same particles at 99% RH (i.e., similar to that inside the human respiratory system) as follows:

$$g\,(99\%) = \left(1 + \kappa_{\mathrm{HTDMA}}\left(\frac{a_w}{1-a_w}\right)\right)^{1/3}. \tag{S6}$$

In Eq. S6, the water activity of the solution droplet (a_w) is calculated iteratively for 99% RH using Eq. S5.

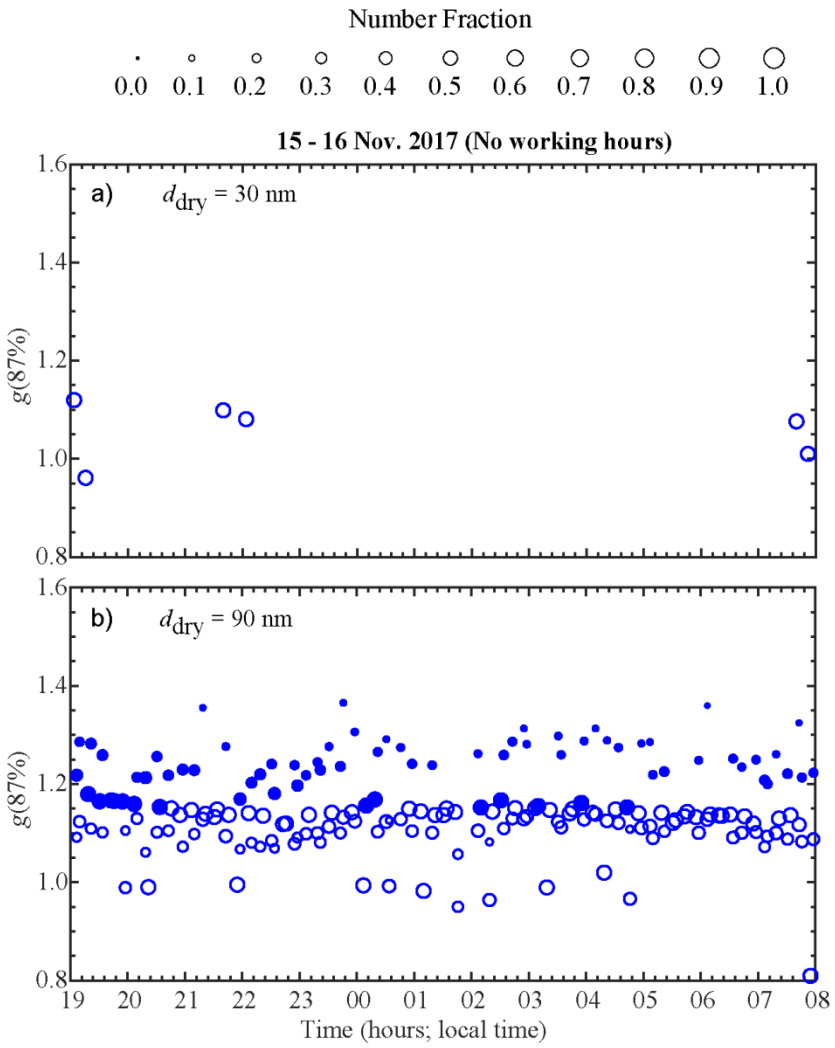

Figure S4. HTDMA measurements of particles having dry mobility diameters of 30- (**a**) and 90- (**b**) nm, sampled from during the non-working hours on 15-16 Nov. 2017. The size of the symbols (i.e., the size of the circles) is proportional to the number fraction of each hygroscopic mode. Particles which exhibited hygroscopic factor below 1.15 (hydrophobic/less hygroscopic; HP) are denoted with different symbols (i.e. open circles), than the more hygroscopic ones (i.e., hygroscopic factor > 1.15; HS).

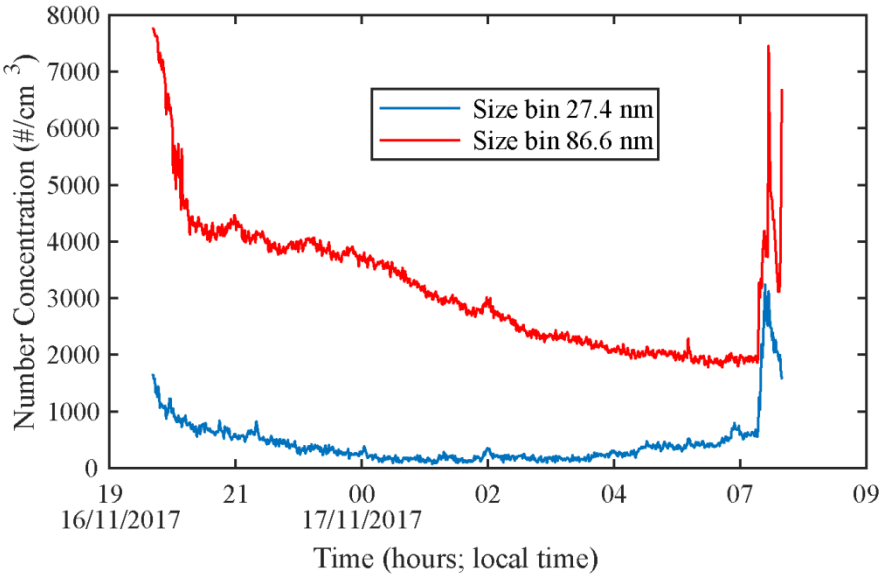

Figure S5. Number concentrations of particles classified by the NanoScan-SMPS as having midpoint electrical mobility diameters of 27.4 and 86.6 nm, measured during the non-working hours between 16 and 17 Nov. 2017. These size bins were selected due to their proximity to dry electrical mobility diameters selected by the HTDMA (i.e., 30 and 90 nm, respectively).

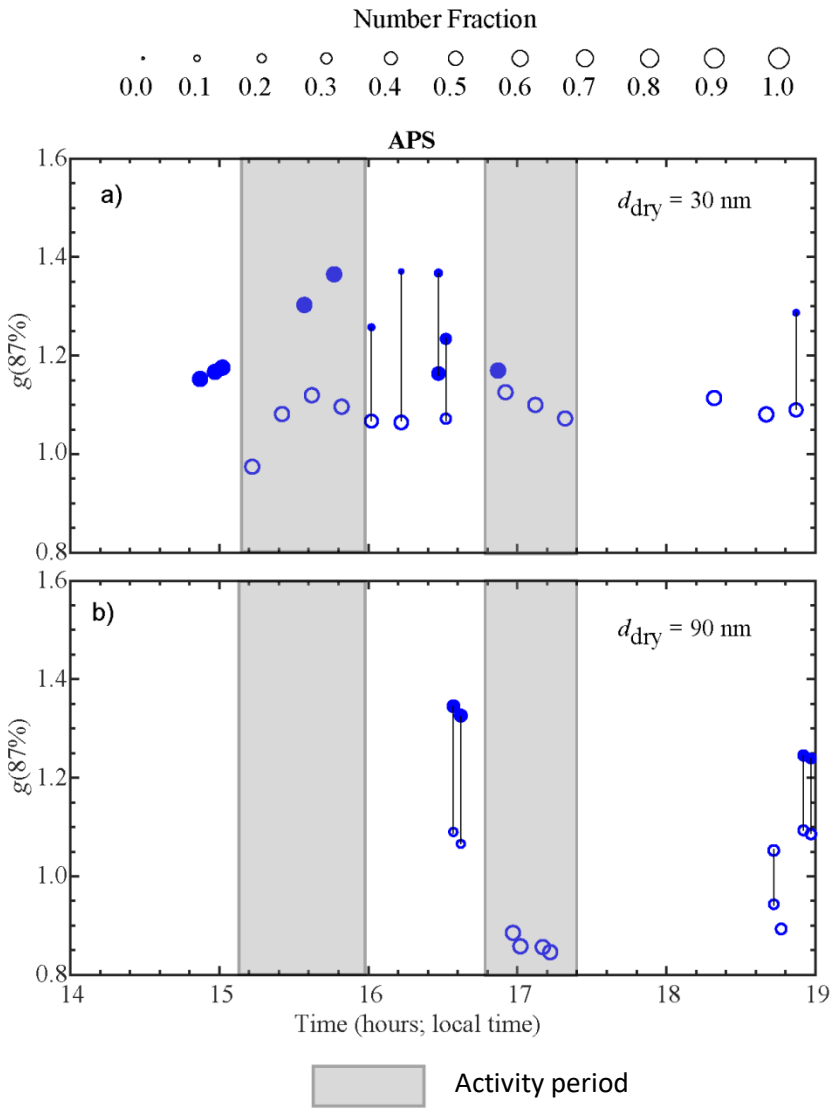

Figure S6. HTDMA measurements of particles having dry mobility diameters of 30 nm (**a**) and 90 nm (**b**), sampled from within spraying booth #1 (APS). The size of the circles is proportional to the number fraction of each hygroscopic mode. Particles having hygroscopic factors below 1.15 (hydrophobic/less hygroscopic; HP) are denoted with open circles, while closed circles denote particles with hygroscopic factors above 1.15 (hygroscopic). Vertical lines, added for clarification reasons, denote externally mixed samples, while the shaded areas mark time intervals during activity periods.

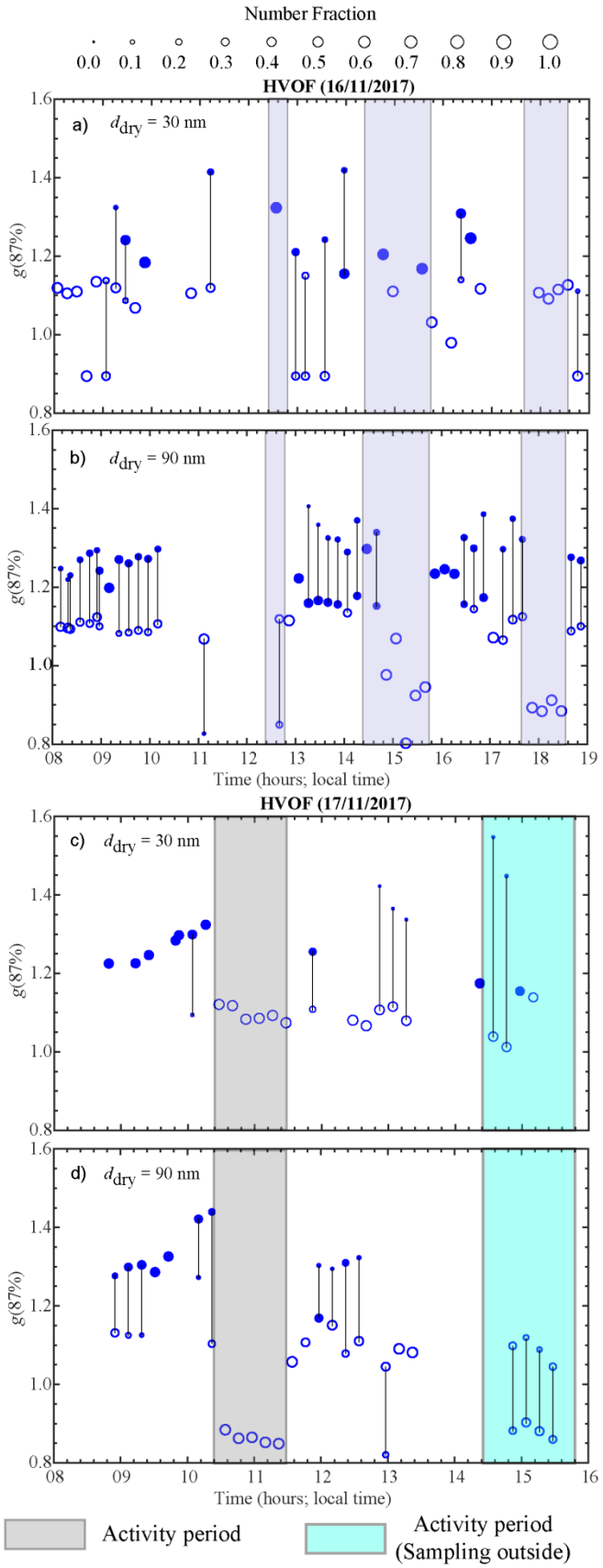
Number Fraction
0.0 0.1 0.2 0.3 0.4 0.5 0.6 0.7 0.8 0.9 1.0
HVOF (16/11/2017)
a) d_{dry} = 30 nm
b) d_{dry} = 90 nm
g(87%)
Time (hours; local time)
HVOF (17/11/2017)
c) d_{dry} = 30 nm
d) d_{dry} = 90 nm
Activity period
Activity period (Sampling outside)

Figure S7. HTDMA measurements of particles having dry mobility diameters of 30- (**a, c**) and 90- (**b, d**) nm, sampled from within booth #3 (HVOF) on 16 and 17 Nov. 2017. The size of the symbols (i.e., the size of the circles) is proportional to the number fraction of each hygroscopic mode. Particles which exhibited hygroscopic factor below 1.15 (hydrophobic/less hygroscopic; HP) are denoted with different symbols (i.e. open circles), than the more hygroscopic ones (i.e., hygroscopic factor > 1.15; HS). Vertical lines, added for clarification reasons, denote externally mixed samples, while the shaded areas mark time intervals during activity periods and the period when the HTDMA was sampling from the storage area, outside booth #3, while it was active.

a)

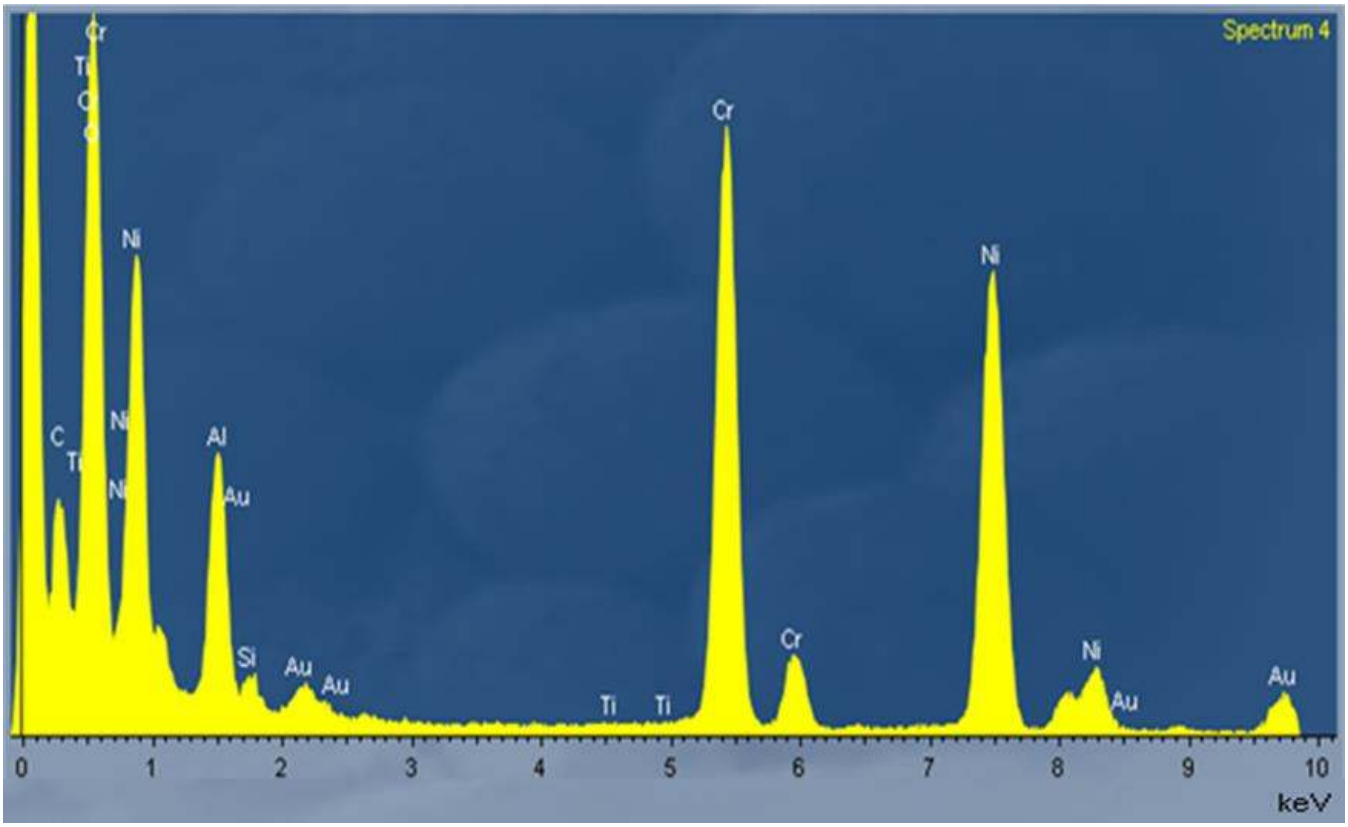

b)

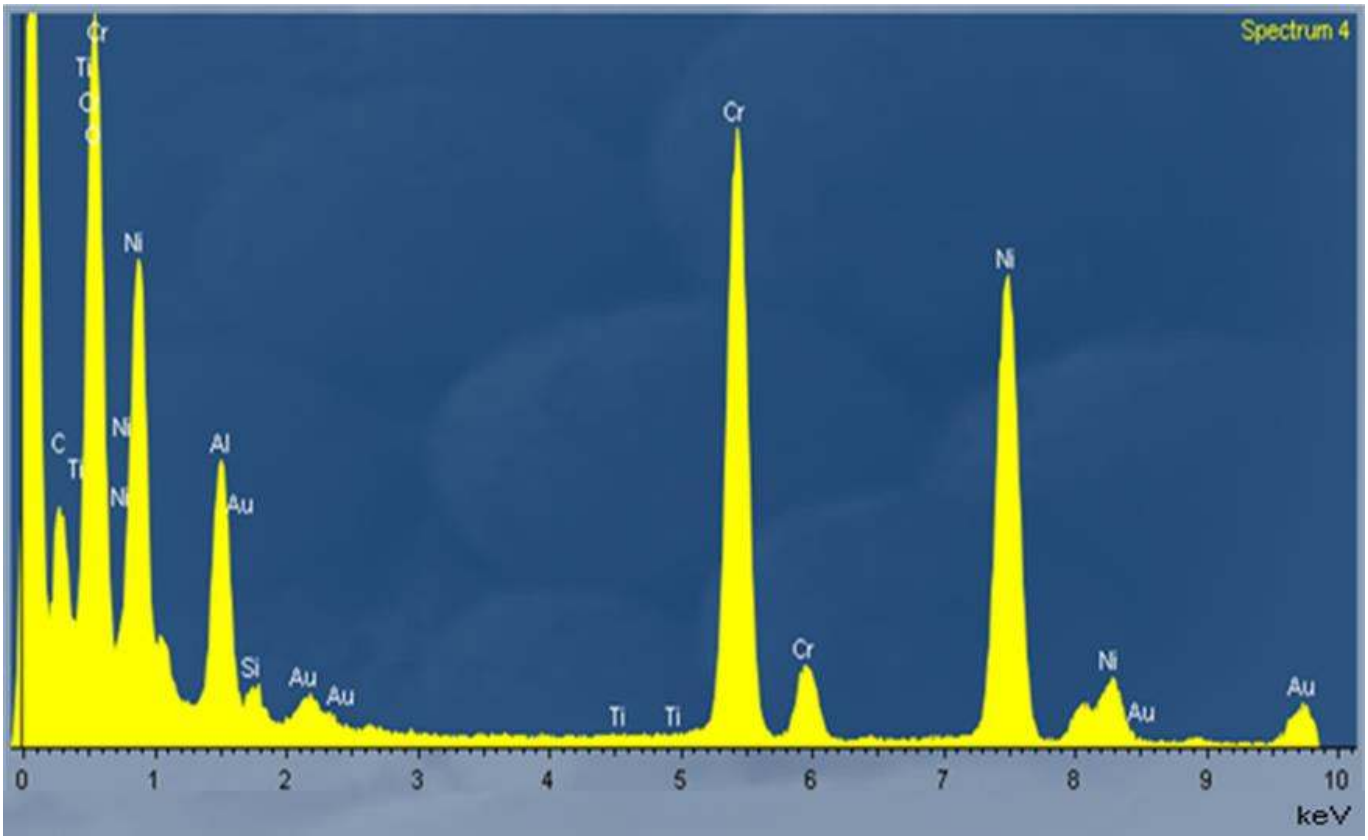

Figure S8. EDX analysis from the respective TEM samples of emitted UFP from (a) APS and (b) HVOF

REFERENCES:

Allen, M. D and Raabe O. G. Slip correction measurements of spherical solid aerosol particles in an improved Millikan apparatus. Aerosol Sci. Technol., 4:269-286, 1985.

Baron P. A and Willeke,K. Aerosol Measurement: Principles, Techniques and Applications. Second Edition, Willey-InterScience, Inc., 2001.

Davies, C. N. Definitive Equations for the Fluid Resistance of Spheres. *Proc. Phys. Soc*., 57:259–270, 1945.

Hinds, W.C. *Aerosol Technology.* New York: John Willey and Sons, 1999.

Kreidenweis, S.M., Petters, M.D., DeMott, P.J.: Single parameter estimates of aerosol water content, Environ. Res. Lett., 3, 035002, 2008.

Petters, M.D. & Kreidenweis S.M.: A single parameter representation of hygroscopic growth and cloud condensation nucleus activity, Atmos. Chem. Phys., 7, 1961-1971, 2007.